Figure 2 shows $E_\Delta(\mathbf{q})$ for a succession of times Δ from 20 to 110 ms. From the low-q data, we find $D_{\text{eff}} = 2 \times 10^{-9}\ \text{m}^2\ \text{s}^{-1}$, so the timescale ranges from $0.3(b^2/2D_{\text{eff}})$ to $1.8(b^2/2D_{\text{eff}})$. A coherence peak at $q \approx (16\ \mu\text{m})^{-1}$ is clearly visible at values of Δ sufficiently large ($\geq$70 ms) for the molecules to diffuse from the starting pore to a first neighbour.

A quantitative fit to the data is possible using equation (3). A simple approximation to $C(Z, \Delta)$ is to assume a gaussian envelope[6], but a more precise description can be made if we consider the cumulative effects or successive pore hops. This pore-hopping formalism yields an approximate closed-form expression for $E_\Delta(q)$ in the case of the pore glass, namely

$$E_\Delta(q) = |S_0(q)|^2 \times \exp\left[-\frac{6D_{\text{eff}}\Delta}{b^2+3\xi^2}\left(1-\exp(-2\pi^2 q^2 \xi^2)\frac{\sin(2\pi qb)}{2\pi qb}\right)\right] \quad (4)$$

where b is the mean and ξ the standard deviation of the distance from the starting pore to the nearest-neighbour pore shell. A more detailed description of pore-hopping theory will be published elsewhere. Figure 3 shows the data for $\Delta = 70$ ms, together with a theoretical curve obtained by using equation (4) in a nonlinear least-squares fit. For simplicity, the form factor chosen corresponds to a spherical pore of diameter a and is thus rather unrealistic. Nonetheless, the fit is fairly good and yields structural parameters $b = 16.1\ \mu\text{m}$, $a = 5.6\ \mu\text{m}$ and $\xi = 2.85\ \mu\text{m}$, which correspond to the physical dimensions of the packed sphere array.

We have performed an inverse Fourier transformation on the $\Delta = 110$-ms data of Fig. 2, using three-dimensional projection reconstruction and assuming the system to be isotropic. This gives an 'image' of the spherically averaged autocorrelation function for the pores convoluted with the diffusion-weighted three-dimensional lattice correlation function (as opposed to the projection, $L(Z)$, of this function along a single axis). Figure 4 shows a slice through the centre of this three-dimensional 'image'.

For the q-space imaging of dynamic displacements, the entire sample contributes to the 'image' signal-to-noise ratio; the resolution is limited only by the available magnitude of $\mathbf{q}$. This is in contrast to NMR imaging in k-space, where increasing the resolution by increasing the imaging gradient results in a deteriorating signal-to-noise ratio in each volume element of the 'image'. We envisage that q-space imaging could realistically achieve sub-micrometre resolution.

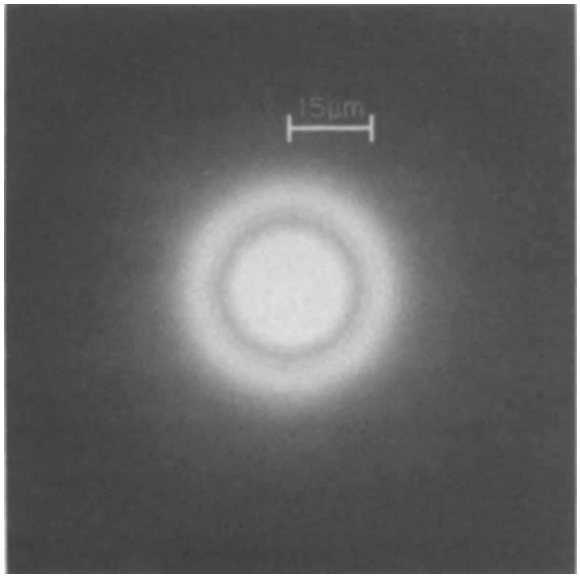

FIG. 4 'Image' of the pore autocorrelation function convoluted with the diffusion-weighted three-dimensional lattice correlation function. The 'image' was obtained by Fourier transformation of the 110-ms data of Fig. 2. The bright inner circle and the first bright ring correspond to the starting pores and the first-neighbour pore shells of the 16-μm spheres respectively.

The observation of a coherence peak as the gradient is increased in a PGSE experiment is remarkable and completely contrary to the usual expectation of monotonically decreasing $E_\Delta(\mathbf{q})$ with increasing $\mathbf{q}$. Such a peak arises because of structural features in the porous solid. A significant number of molecules moving one pore spacing suffer no net phase shift when $qb \approx 1$. We are unaware of any previous measurement in which $E_\Delta(\mathbf{q})$ increases with increasing $\mathbf{q}$. □

Received 21 January; accepted 16 April 1991.

1. Stejskal, E. O. & Tanner, J. E. *J. chem. Phys.* **42,** 288–292 (1965).
2. Callaghan, P. T. *Aust. J. Phys.* **37,** 359–387 (1984).
3. Stilbs, P. *Prog. nucl. magn. Resonance Spectrosc.* **19,** 1–45 (1987).
4. Mansfield, P. & Grannell, P. K. *Phys. Rev.* **B12,** 3618–3634 (1975).
5. Cory, D. & Garroway, A. *Magn. Resonance Medicine* **14,** 435–444 (1990).
6. Callaghan, P. T., MacGowan, D., Packer, K. J. & Zelaya, F. O. *J. magn. Resonance* **90,** 177–182 (1990).
7. Kärger, J. & Heink, W. *J. magn. Resonance* **51,** 1–7 (1983).
8. Haughey, D. P. & Beveridge, G. S. G. *Can. J. chem. Engng* **47,** 130–140 (1969).
9. Graton, L. C. & Fraser, H. J. *J. Geol.* **43,** 785–909 (1935).

ACKNOWLEDGEMENTS. We thank D. Cory for advice on the polymer sphere system used in this work.

Air entrainment and dissipation in breaking waves

Eric Lamarre & W. K. Melville

R. M. Parsons Laboratory, Department of Civil Engineering, Massachusetts Institute of Technology, Cambridge, Massachusetts 02139, USA

WAVE breaking transfers momentum from the atmosphere (winds) to the ocean (currents)[1,2] and entrains air in bubbles which are believed to generate and scatter underwater sound[3–5]. Wave breaking and the associated entrainment of air in bubbles are also thought to be important in heat and gas transfer across the air–sea interface[6–8], but the lack of detailed measurements of air entrainment in bubbles has impeded our understanding of the effect of wave breaking on these processes. Here we present measurements of air entrainment by controlled deep-water breaking waves, which show that the bubble plumes generated by breaking waves contain volume fractions of air that are many orders of magnitude greater than expected. Bubble plumes with such large void fractions may be the source of low-frequency sound in the ocean[9]. We conclude that the processes of surface-wave evolution and air entrainment are dynamically coupled, and that the contribution of bubbles to air–sea gas transfer and to sound propagation may be seriously underestimated if the existence of these plumes of large bubbles is not taken into account.

Experiments were conducted in a wave channel 25-m long and 0.7-m wide filled with fresh water to a depth of 0.6 m. The experiment consisted of generating breaking waves and mapping the bubble plume created by breaking for three different amplitudes of the same wave packet (see Table 1 for wave-packet characteristics). The breaking waves were produced by a piston-type wavemaker. Details of wave generation and photographs of breaking waves are given by Rapp and Melville[2]. The technique gives very repeatable wave profiles and energy dissipation, and we found it to give fairly repeatable bubble plumes. The volume fraction of air (void fraction, given in % hereafter) in an air–water mixture can be measured by making use of the large difference in electrical conductivity between air and water. This technique has been used in closed-conduit two-phase flows,

and reviews can be found in the literature[10,11]. We used essentially the same technique to map the void-fraction distribution in bubble plumes generated by breaking waves. Typical wave-gauge and void-fraction time series are shown in Fig. 1. Additional details of the probe and the experimental procedures will be published elsewhere.

Contour maps showing the evolution of the void-fraction distribution can be assembled from the individual time series (Fig. 2). Measurements over the full range 0–100% of void fractions have been observed, and void fractions of >20% for all three wave amplitudes were sustained for up to half a wave period after breaking. These measurements show that the volume fractions of air near the surface within one wave period following breaking are many orders of magnitude greater than the time-averaged (over ~10 min) values measured in the field[12]. It is well known that the speed of sound in water can be reduced by an order of magnitude in the presence of void fractions as low as 1%. Our results therefore suggest caution in using time-averaged void-fraction measurements to infer sound propagation through the surface bubble layer (which acts as an acoustic waveguide[13]).

The important parameters describing the bubble plume are presented in Fig. 3. The total volume of entrained air, V, shown in Fig. 3*a* is computed from

$$V = b \int_A \alpha \, dA \qquad (1)$$

where α is the local void fraction, b is the channel width and A is the cross-sectional area of the bubble plume. The volume of air enclosed in the initial air pocket is conserved for up to a quarter of a wave period after breaking. Degassing of the plume is very rapid, with only 5% of the initially entrained air remaining after a full wave period. The fast rising speed of large bubbles (radius >1 mm) must account for most of the air lost in the first wave period. Laboratory wind-flume experiments[14] have shown the contribution to total flux of carbon dioxide by bubbles to be almost independent of radius in the range 0.02–2 mm despite the fact that larger bubbles are less numerous and have a shorter underwater residence time. The very fast degassing rate of the bubble plume revealed by our experiments indicates that modelling of the contribution of bubbles to total air–sea gas transfer may be considerably underestimated if the transient large bubble population (radius ~1–10 mm) is not considered.

The cross-sectional area of the bubble plume is shown in Fig. 3*b*. The void-fraction gauge used in our experiments is insensitive to void fractions lower than 0.3%. We expect the initial rise in bubble-plume area to be essentially independent of the void-fraction detection threshold, giving an area expansion rate of $28V_0/bT$ (where T is the characteristic wave period) for the time between 0.1 to 0.3T. We expect that the rate of decrease of A would be lower in the later stages (after the peak value) if a lower threshold were attainable with the instrument.

The mean void fraction is given by $\bar{\alpha} = V/bA$ (Fig. 3*c*). Mean void fractions in the bubble plume remain above 1% within the first wave period after breaking. Important changes in the speed of sound are associated with these localized distributions of large void fractions. Such discontinuities have been suggested previously as a possible source of low-frequency sound (<1 kHz) in the ocean[15]. Our results indicate that these large discontinuities exist in the laboratory and are likely to be found in the field.

The work required to keep the air entrained against the buoyancy force is

$$E_b = \rho g b \int_A \alpha z \, dA \qquad (2)$$

where ρ is the water density, g is the acceleration due to gravity and z is the vertical distance to the free surface. Normalizing

TABLE 1 Characteristics of the three wave amplitudes studied.

ak	t_b (s)	x_b (m)	E_w/b (J m^{-1})	E_d/b (J m^{-1})	V_0 (cm^3)	$E_d/\rho g V_0 \lambda$	Δx (cm)	Δz (cm)
0.54	14.4	8.05	110.0	17.8	6,860	0.10	5	5
0.45	14.3	7.70	78.0	8.6	3,220	0.10	5	5
0.38	14.3	7.70	58.7	4.3	1,750	0.09	5	5

The slope of the packet[2] is given by ak. The centre frequency of the wave packet and the bandwidth were both 0.88 Hz. The time from initial motion of the piston is t_b, and x_b is the breaking location downstream of the piston. Both t_b and x_b are defined by the time at which the forward-moving jet strikes the free surface and an air pocket is formed. The volume of the air pocket at $t = t_b^+$ is V_0 (measured from video images at t_b; because of lack of video resolution for ak = 0.38, V_0 was taken as the maximum V measured). E_w is the total pre-breaking wave energy, E_d the total energy dissipated by breaking[2]. $E_d/\rho g V_0 \lambda$ is the ratio of wave energy dissipated to the maximum volume of air entrained normalized by the specific weight of water ρg and the characteristic wavelength λ. The horizontal and vertical resolutions of the void-fraction measurements are Δx and Δz. The channel width, water density and gravity are b, ρ and g.

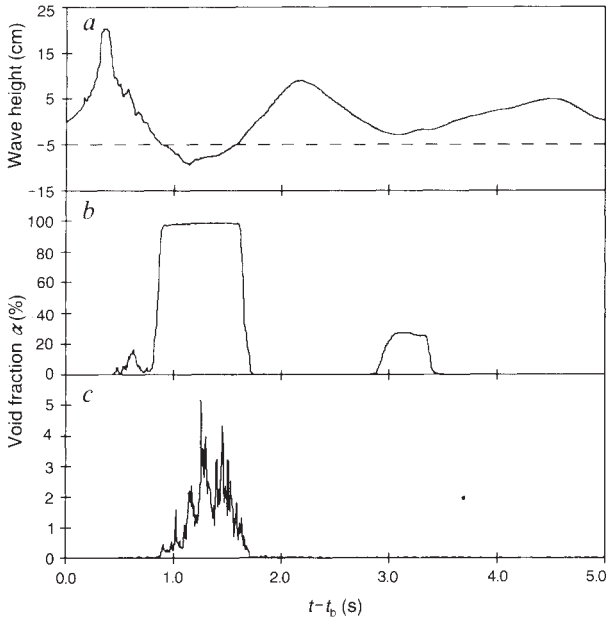

FIG. 1 Typical time series at 200 Hz of *a*, wave-gauge measurements; *b*, *c*, void-fraction measurements at depths −5 cm and −15 cm, respectively, from the still-water level. All data are for the most energetic breaker studied at 0.55 m downstream of x_b. Note how the probe crosses the water surface at 0.8 s in *b*. 'Surface effect' is shown in *b* at 3 s. The second wave trough has its water surface at ~−2.5 cm and therefore intrudes into the measuring volume of the void-fraction gauge which is located at −5±3 cm. The effective measuring volume of the probe was a horizontal cylinder ~20 cm long and ~6 cm in diameter.

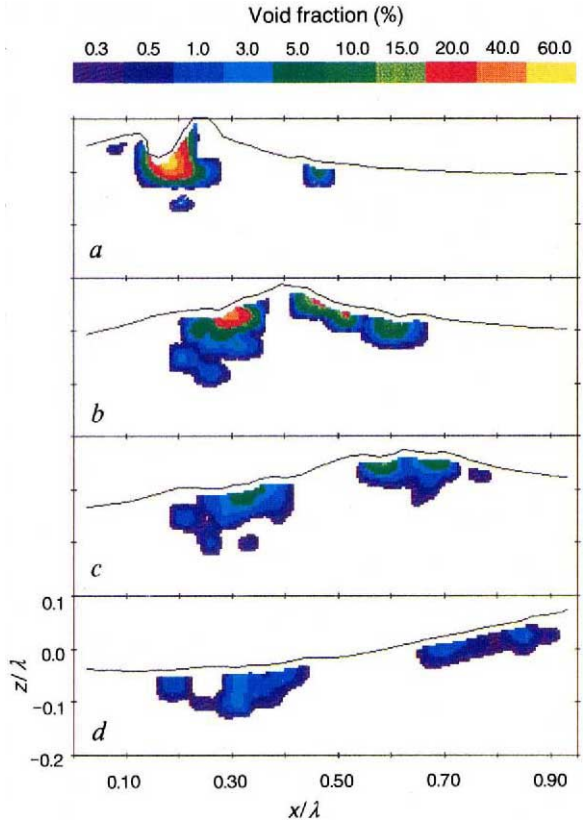

FIG. 2 Contour maps of void fractions for the most energetic breaker studied. Time increases from *a* to *d*. Times from breaking, $t-t_b$, are 0.3, 0.5, 0.7 and 1.0 s; times normalized by the wave period, $(t-t_b)/T$, are 0.26, 0.44, 0.62 and 0.88 respectively. The wave moves from left to right. Each frame is constructed from ~170 ensemble averages of three runs. Note the distinct downstream cloud generated by the splash from the initial impact at breaking.

the data by the total wave energy dissipated by breaking, E_d, gives a simple exponential form (Fig. 3*d*). Up to 40% of the total prebreaking wave energy can be lost through breaking[1]; our data now show that a large fraction (30–50% and maybe more) of the energy lost is expended in entraining the bubble plume. This is direct evidence that the processes of surface wave evolution and air entrainment have considerable dynamical coupling. The near-constant ratio $E_d/\rho g V_0 \lambda$ for these experiments, as shown in Table 1, implies that the initial volume of air entrained correlates with the energy dissipated. Recent studies[16,17] have shown that the wave energy dissipated correlates with the acoustic energy radiated and the backscattering of microwave by radar breaking waves. Thus our measurements suggest that it may be possible to quantify air entrainment and gas transfer in the field using acoustic and microwave techniques.

The horizontal and vertical centroids of the void-fraction distribution in the bubble plume $\bar{x}$ and $\bar{z}$, respectively, are

$$(\bar{x}, \bar{z}) = \frac{\int_A \alpha(x, z)\, dA}{\int_A \alpha\, dA} \qquad (3)$$

where x is the horizontal distance from x_b and z is the depth from the free surface. The horizontal centroid in Fig. 3*e* moves at roughly the phase speed of the wave for a period $T/2$. In field studies[5] using sonar, it was found that the cloud in the

FIG. 3 *a*, Air volume V normalized by V_0. The data for the three waves collapse onto a simple decaying exponential, $V/V_0 = 2.6\exp(-3.9(t-t_b)/T)$. *b*, Cross-sectional area A of bubble plume normalized by V_0/b. The data were fitted by using the functional form for V/V_0 divided by that for $b\bar{\alpha}$. (This procedure was used because extrapolation of the curves for V and $\bar{\alpha}$ is evidently better conditioned than extrapolation of the data for A directly.) The fitted curve has equation $Ab/V_0 = 325((t-t_b)/T)^{2.3}\exp(-3.9(t-t_b)/T)$. *c*, Mean void-fraction $\bar{\alpha}$. The data are fitted well by a power law, $\bar{\alpha}(\%) = 0.8((t-t_b)/T)^{-2/3}$ with $\alpha = 100\%$ near $t = 0$, as one would expect for the initial air pocket. *d*, Potential energy E_b of the bubble plume, normalized by E_d. Data are fitted with a decaying exponential, $E_b/E_d = 0.7\exp(-3.6(t-t_b)/T)$. *e*, *f*, Void-fraction centroids in bubble plume normalized by the wavelength. *e*, Horizontal centroid $\bar{x}$. Solid line is phase speed of the wave, $c = \lambda/T$. *f*, Vertical centroid $\bar{z}$. Note that the vertical centroid does not increase monotonically with ak. Time in all six plots is normalized by the wave period T. Symbols for the three waves: ○, ak = 0.54; □, ak = 0.45; △, ak = 0.38.

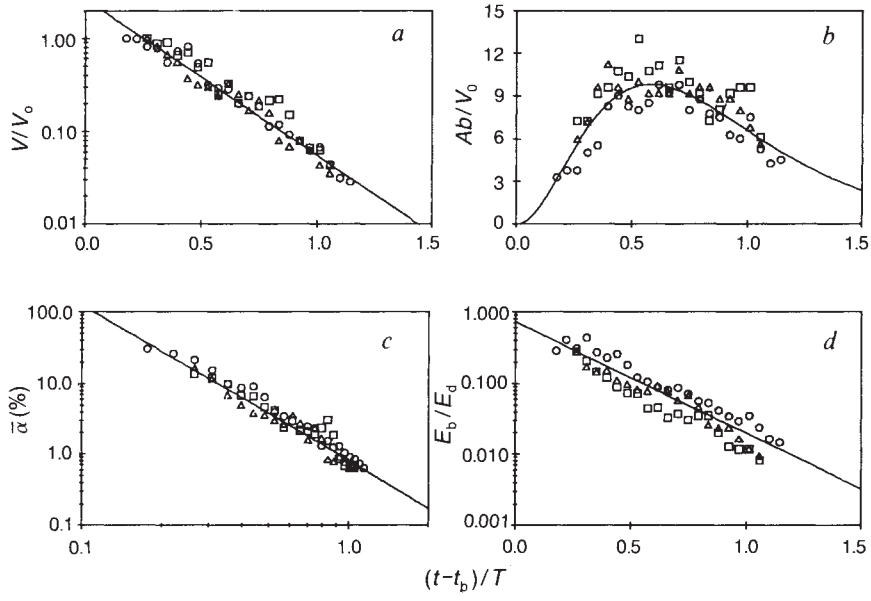

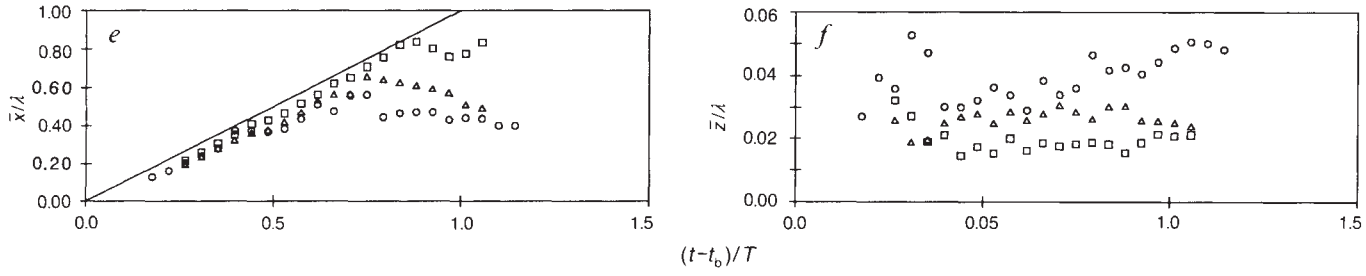

early stage after breaking moved at the wind-wave phase speed. The above results are consistent with these findings. The vertical centroid for each packet shown in Fig. 3*f* is roughly constant, but values for different packets range between 0.015λ and 0.05λ where λ is a characteristic wavelength. This suggests that, at least in the first wave period, the downward advection of fluid may balance the upward motion of the bubbles themselves.

We have shown that the bulk properties of the bubble plume generated by breaking waves scale with the prebreaking wave variables and evolve according to simple functions of time. The close dynamical coupling between wave breaking and air entrainment suggests that models of air–sea gas transfer could be improved by better characterization of breaking surface waves, perhaps through remote sensing methods[17]. □

Received 16 November 1990; accepted 15 April 1991.

1. Melville, W. K. & Rapp, R. J. *Nature* **317,** 514–516 (1985).
2. Rapp, R. J., Melville, W. K. *Phil. Trans. R. Soc.* **A331,** 735–800 (1990).
3. Medwin, H. & Daniel, A. C. *J. acoust. Soc. Am.* **88,** 408–412 (1990).
4. Medwin, H. & Beaky, J. *J. acoust. Soc. Am.* **86,** 1124–1130 (1989).
5. Thorpe, S. A., Stubbs, A. R. & Hall, A. J. *Nature* **296,** 636–638 (1983).
6. Thorpe, S. A. *Nature* **318,** 519–522 (1985).
7. Merlivat, L. & Memery, L. *J. geophys. Res.* **88,** 707–724 (1983).
8. Watson, A. J., Upstill-Goddard, R. C. & Liss, P. S. *Nature* **349,** 145–147 (1991).
9. Lu, N. Q., Prosperetti, A. & Yoon, S. W. *IEEE J. Ocean Eng.* **15,** 275–281 (1990).
10. Olsen, H. O. thesis, Kjeller Research Establishment (1967).
11. Bernier, R. N. thesis, Calif. Inst. Tech. (1981).
12. Walsh, A.L. & Mulhearn, P.J. *J. geophys. Res.* **92,** 14553–14565 (1987).
13. Farmer, D. M. & Vagle, S. *J. acoust. Soc. Am.* **86,** 1897–1908 (1989).
14. Broecker, H. Ch., & Siems, W. in *Gas Transfer at Water Surfaces* (eds Brutsaert, W. & Jirka, G.H.) (Reidel, Dordrecht, 1984).
15. Prosperetti, A. in *Sea Surface Sound* (ed. Kerman, B.R.) 151–171 (Kluwer, Dordrecht, 1987).
16. Melville, W. K., Loewen, M. R., Felizardo, F. C., Jessup, A. T. & Buckingham, M. J. *Nature* **336,** 54–59 (1988).
17. Loewen, M. R. & Melville, W. K. *J. Fluid Mech.* **224,** 601–623 (1991).

ACKNOWLEDGEMENTS. We thank W. H. Huang for assistance in designing and constructing equipment. This work is supported by the Office of Naval Research (Ocean Acoustics) and the NSF (Physical Oceanography).

Constraints from noble-gas contents on the origin of carbonado diamonds

M. Ozima*†, S. Zashu*, K. Tomura‡ & Y. Matsuhisa§

* Department of Geophysics, University of Tokyo, Tokyo 113, Japan
‡ Institute for Atomic Energy, Rikkyo University, Yokohama 240-01, Japan
§ Geological Survey of Japan, Tukuba-City, 305, Japan
† Present address: Department of Earth and Space Science, Osaka University, Toyonaka City, 560, Japan

CARBONADOS are porous aggregates of micrometre-size diamond crystals[1,2]. Although they are not rare, they have not been found in kimberlites[3], and they contain inclusion minerals typical of the Earth's crust, rather than the upper-mantle assemblages commonly found in kimberlite diamonds. Carbonados also have lower $^{13}C/^{12}C$ ratios than kimberlite diamonds[1,2,4]. Although these observations strongly suggest that carbonados were formed in the crust, crustal conditions are generally unlikely to provide pressures and temperatures in the diamond stability field (but see ref. 5 for a possible exception). Other suggestions for the origin of carbonado include the transformation of subducted carbon in the mantle[6], impact metamorphism of crustal rocks containing organic carbon[7], and (for very fine-grained carbonado) the irradiation of organic matter by decaying uranium and thorium in uranium-rich phases[8–10]. Here we present further evidence for a crustal connection, in the form of noble-gas data for four carbonados from Brazil and Africa. We find that all four contain large amounts of implanted xenon and krypton from ^{238}U fission, nucleogenic neon and ^{4}He, and tightly trapped atmospheric noble gases, from which we conclude that these carbonados formed in a uranium-rich crustal environment.

We studied two carbonados from Brazil and two from Africa, all from different localities. Before the noble gas experiments, samples were thoroughly cleaned with hot HNO_3 and HF. Noble gases were extracted by heating the samples at temperatures up to 2,000 °C (graphitization temperature is 1,900 °C) and analysed by mass spectrometry. Table 1 gives the analytical data and details of the method. The isotopic compositions of neon, krypton and xenon are distinctly different from those in the atmosphere. The extraordinary neon isotope ratios can be attributed to nuclear reactions (Wetherill reactions)[11] such as $^{18}O(\alpha, n)^{21}Ne$ and $^{19}F(\alpha, n)^{22}Ne$. Assuming that ^{130}Xe, ^{80}Kr and ^{20}Ne are entirely atmospheric, we calculated the excess of the isotopes ^{136}Xe, ^{86}Kr and ^{21}Ne in the samples relative to the values expected if the ratios were atmospheric. We show these in Table 2 together with their uranium and ^{4}He contents, and $\delta^{13}C$ values. The excess Xe and Kr isotopes must arise from fission of ^{238}U, and are given the subscript 'fission' in the table. In Fig. 1, we plot $^{136}Xe/^{132}Xe$ against $^{134}Xe/^{132}Xe$ obtained when the African sample 90706P was degassed by step-heating: the data show that Xe in the diamond is a mixture of atmospheric Xe and Xe arising from ^{238}U fission. Published values[12] of the production ratios for $^{4}He/^{136}Xe$ and $^{136}Xe/^{86}Kr$ in spontaneous fission of ^{238}U are 0.3×10^{9} and 6.0 respectively. These are well within the range for the observed ratios of $0.27–0.8\times10^{9}$ and 3.8–12.6. Table 2 also shows the amounts of nucleogenic ^{136}Xe,

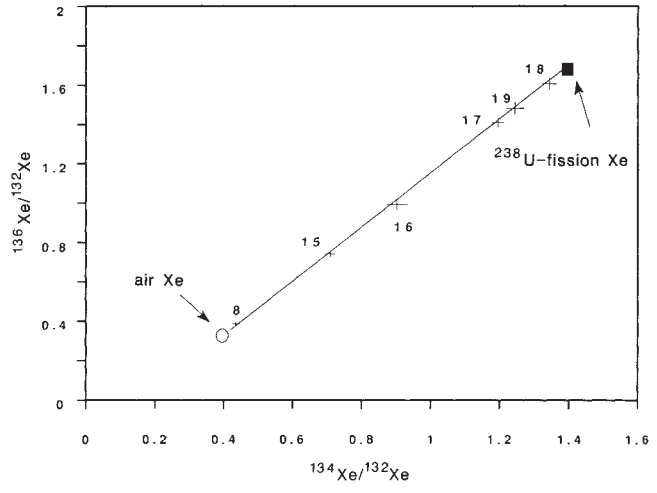

FIG. 1 Step-heating data for Xe. The ratio $^{136}Xe/^{132}Xe$ is plotted against $^{134}Xe/^{132}Xe$ to form a three-isotope plot. The numbers indicate step-heating degassing temperatures (in 100 °C). Sample, Africa 90706P. This sample was prepared by pulverizing a diamond from the same batch as sample 90706 to fine powder (<10 μm), and thoroughly cleaned with hot HF and HNO_3 to remove possible contaminants. Note that all data lie on a mixing line between atmospheric Xe and ^{238}U fission Xe.